INFLUENCE OF THE RF VOLTAGE AMPLITUDE ON THE SPACE-AND TIME-RESOLVED PROPERTIES OF RF-LF DIELECTRIC BARRIER DISCHARGES IN α–γ MODE

Raphaël Robert, Nader Sadeghi, Gerjan Hagelaar, Luc Stafford, Françoise Massines

INFLUENCE OF THE RF VOLTAGE AMPLITUDE ON THE SPACE- AND TIME-RESOLVED PROPERTIES OF RF-LF DIELECTRIC BARRIER DISCHARGES IN α-γ MODE

Raphaël Robert[1,2], Nader Sadeghi[3], Gerjan Hagelaar[4], Luc Stafford[2], Françoise Massines[1]

[1]Laboratoire Procédés Matériaux et Énergie Solaire (PROMES, CNRS, UPR 8521), Rambla de la thermodynamique, 66100 Perpignan, France

[2]Département de physique, Université de Montréal, 1375 ave. Thérèse-Lavoie-Roux, Montréal, Québec, H2V 0B3, Canada

[3]Laboratoire Interdisciplinaire de Physique (LIPhy CNRS, UMR 5588), Université de Grenoble-Alpes, Grenoble, France

[4]Laboratoire Plasma et Conversion d'Énergie (LAPLACE, CNRS, UMR5213), 118 Route de Narbonne, 31077 Toulouse, France

Abstract

This work reports the results of an experimental and modelling study on dual-frequency Ar-NH_3 dielectric barrier discharges (DBD) exhibiting the α – γ transition. A combination of space- and time-resolved optical absorption and emission spectroscopy is used to record spatio-temporal mappings of the Ar metastable number density, Ar 750.4 nm line emission intensity, and electron-Ar Bremsstrahlung continuum emission intensity. With the increase of the RF voltage amplitude in a 50 kHz-5 MHz DBD, maximum populations of Ar excited species (1s and 2p states, linked to the population of high-energy electrons) observed in the γ mode decrease and appear earlier in the low-frequency cycle. On the other hand, the density of the bulk electrons, monitored from the continuum emission intensity, increases, with a more prominent rise in the RF-α mode than in the γ regime. Such behaviors are consistent with the predictions of 1D fluid model and results from a decrease of the gas voltage required for self-maintenance of the cathode sheath in the γ breakdown.

1. Introduction

Since the 1990's, low-pressure dual-frequency plasmas have been developed. First studied for precursor dissociation rate control in deposition and etching processes, the association of a radio frequency (RF) and a microwave voltage [1]–[6], or two RF voltages [7], [8], [17]–[24], [9]–[16], is now a common method to tailor the ion energy distribution function (IEDF) on plasma-exposed surfaces, independently of the ion flux [17], [20], [21], [25]–[29]. In recent developments of dielectric barrier discharges (DBDs) at atmospheric pressure for a number of applications, in particular for thin-film deposition [30]–[33], a RF voltage is often associated with a low frequency (LF) one (between 1 and 500 kHz) [30], [31], [40], [41], [32]–[39] or with another RF [28], [29], [42]–[46]. In such conditions, dual-frequency discharges increase the power absorbed (and dissipated) by the plasma electrons, while maintaining an homogeneous discharge mode [30], [34]–[36], [40], [41]. Hence, the number densities of charged and reactive species significantly increase [38].

RF-LF dual-frequency discharges operated in Ar-based gases at atmospheric pressure can reveal unique features. In particular, during an LF period, depending on the amplitude of the LF voltage, it is possible to observe an alternation between 2 typical RF discharge conditions: the α regime and the γ regime [31], [32], [38], [39], [43], [45]. On one hand, when the LF voltage applied to the gas is low enough, the discharge exhibits a RF-α behavior, characterized by an ohmic heating of plasma electrons in the bulk [13], [29], [44]. On the other hand, when the amplitude of the LF voltage is almost maximum, and of the same polarity as the RF voltage, the secondary electrons created at the electrode become accelerated by the electric field present in the sheath and a self-sustainment criterion in the sheath is established; this is the γ regime [39]. In recent studies, this so-called α – γ transition was found to depend on a number of operating parameters, including the amplitude of the LF voltage [38], the amplitude of the RF voltage [31], and the relative concentration of NH_3 in Ar-NH_3 Penning gas mixtures [39]. In this work, space- and time-resolved optical emission spectroscopy,

combined with tunable diode laser absorption and fluid modeling, are used to examine the influence of the RF voltage amplitude on electron densities, electron temperatures, and populations of Ar metastable atoms in α – γ dual-frequency DBDs operated in Ar-NH_3 Penning gas mixtures. This complete set of data provides new insights into the α – γ transition and highlights the predominant role of dielectrics in DBD conditions.

2. Experimental setup and diagnostics

2.1. DBD reactor

The dual-frequency Ar-based DBD studied in this work is sustained in a plane-to-plane configuration [38]. The gas gap is 2 mm and a 1 mm-alumina-dielectric-layer is placed on each metallic electrode. The DBD cell is located inside an air-tighten chamber, which is first evacuated with a primary vacuum pump down to about 1 mTorr, and is then filled with a Penning mixture of Ar + 200 ppm of NH_3 at a total gas flow rate of 3 SLM (standard liters per minute). A needle valve between the chamber and the pumping system allows fixing the total pressure in the chamber to 760 Torr. Dimensions of the discharge zone are 0.2 x 1 x 5 cm^3. RF and LF voltages are generated by a single-waveform generator (Keysight 33500B Series), allowing their synchronization, and are independently amplified. As in previous studies [38], [39], excitation frequencies are LF 50 kHz and RF 5 MHz. Here, the LF voltage amplitude is set at 650 V, 50 V above the LF breakdown voltage. As for the RF voltage amplitude, it is varied between 0 and 290 V.

2.2. Optical emission spectroscopy

The Ar-based DBD is characterized by time- and space-resolved optical emission spectroscopy using the optical system presented in Figure 1. The plasma light is collected with a 10 cm-focal-length lens,

placed at 15 cm from the center of the DBD cell. Combined with a set of 3 mirrors (forming a periscope), this lens forms the image of a selected region of the discharge on the entrance slit of a Czerny–Turner monochromator (Jobin-Yvon, 66 cm focal length, 1200 groves/mm grating, slit width 150 µm) located at 30 cm optical distance from the lens. Here, the 3-mirrors set, placed between the lens and the monochromator, rotates the image of the discharge zone by 90°. Considering the dimensions of the DBD and neglecting the edge-effect, the density of the excited species in the plasma volume can be assumed to have only a one dimensional variation along the DBD's gap. Thus, the signal light on the slit represents the intensity of the light emission from the plasma layer at a given distance from the electrodes. The periscope is fixed on a micrometric screw such that its movement along the horizontal axis induces the displacement of the image of the discharge gap on the monochromator's slit and thus offers the possibility to probe light emission from different zones of the plasma gap. Considering the factor 1.95 magnification of the image and the 150 µm width of the entrance slit of the monochromator, the spatial resolution within the gap is 77 µm.

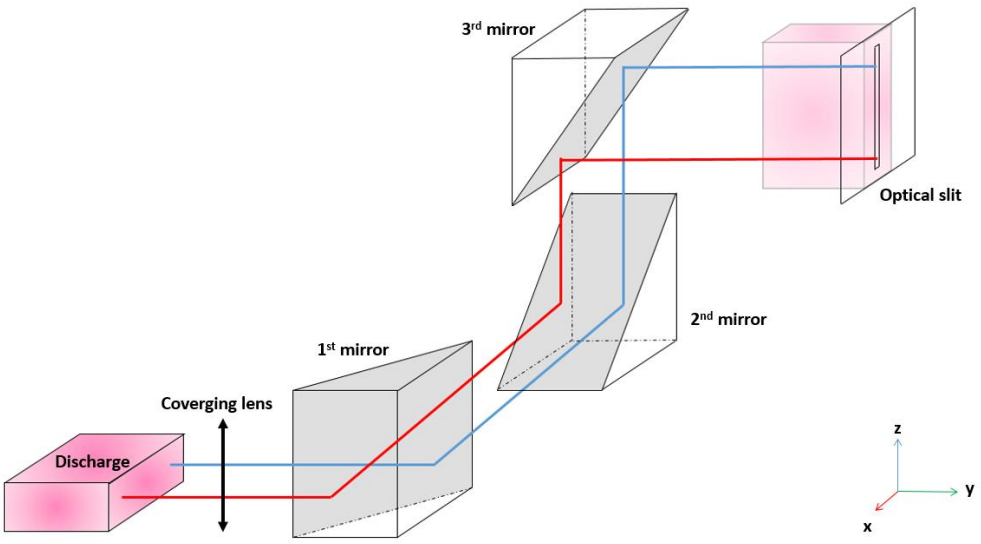

FIGURE 1. OPTICAL SETUP USED FOR MAGNIFICATION, ROTATION, AND SCANNING ALONG THE DISCHARGE GAP OF THE PLASMA LIGHT EMISSION.

The light at the wavelength selected by the monochromator is detected with a Hamamatsu photomultiplier tube (PMT, H10721-20) operating in photon counting mode. A multichannel photon counter (MSC6A2T8 Fast Comtec) is used to record the time variation of the wavelength-selected light emission intensity over the 20 µs cycle of the LF voltage with a time resolution of 6.4 ns. A TTL signal, in phase with the LF voltage from the waveform generator, triggers the photon counter. The photon pulses from the PMT are counted in different channels of the MCS6A2T8 counter according to their respective arrival time after the triggering signal [33]. Averaging the photon signals over 10^6 LF cycles (20 s total acquisition time) provides an excellent signal-to-noise ratio. Data are transferred to a computer for the storage and further treatment, as shown in Figure 2. This phase-resolved optical signal can further be correlated with the discharge current-voltage characteristics [38] acquired with a digital oscilloscope triggered by the same TTL pulse as the MSC6A2T8 multichannel photon counter.

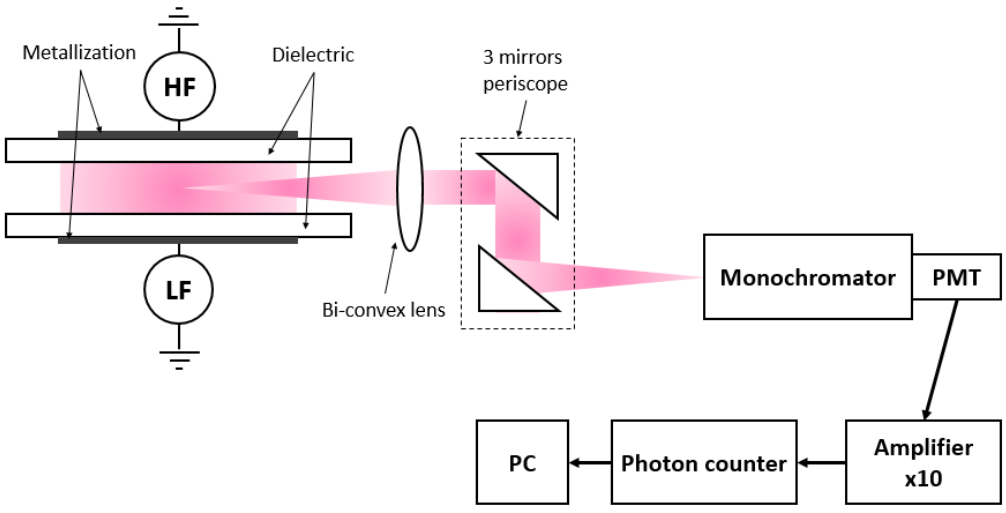

FIGURE 2. EXPERIMENTAL SETUP WITH ALL OPTICAL AND ELECTRICAL COMPONENTS FOR SPACE- AND TIME-RESOLVED OPTICAL EMISSION SPECTROSCOPY.

2.3. Tunable diode laser absorption spectroscopy

The density of Ar metastable atoms in the Ar-based DBD is measured by tunable diode laser absorption spectroscopy with the same equipment and in the same conditions as [47]. A beam from the tunable diode laser, whose wavelength is tuned around 772.4 nm, crosses the DBD discharge volume along its 5 cm longer arm. Due to the closeness of the Ar transitions 772.38 nm ($2p_7 \leftarrow 1s_5$) and 772.42 nm ($2p_2 \leftarrow 1s_3$), and their pressure broadening at 760 Torr, the laser beam can be absorbed by both Ar($1s_5$) and Ar($1s_3$) metastable atoms (Paschen notations are used, corresponding to $4s[3/2]_2$ and $4s[1/2]_0$ metastable states in Racah notation) [48]. However, as the oscillator strength of the $2p_2 \leftarrow 1s_3$ transition is more than an order of magnitude larger than the one of the $2p_7 \leftarrow 1s_5$ transition [48], by setting the laser wavelength at 772.435 nm, which is the peak position of the pressure-shifted $2p_2 \leftarrow 1s_3$ line [49], the absorption signal represents the density of Ar($1s_3$) atoms [47], [49]. The time-resolved number density of Ar($1s_3$) atoms can be deduced from the time-resolved absorption coefficient at 772.435 nm, using relations reported in [49]–[51]. Here, the about 500 µm diameter of the laser beam limits the spatial resolution within the gap but allows to estimate the Ar($1s_3$) atoms density either in the plasma bulk (middle distance from the top and bottom electrodes) or in a zone close to the top electrode, including the sheath edge.

3. Space and time-resolved optical measurements

3.1. Analysis of metastable Ar atoms

Figure 3 shows a typical time variation of the Ar($1s_3$) number density during one LF cycle of the dual-frequency Ar-NH_3 DBD at two positions in the gap: in the bulk at mid-distance between the top and bottom electrodes, and in a zone including the sheath edge, near the top electrode. Applied voltages are V_{LF} = 650 V and V_{RF} = 195 V, and the discharge exhibits the α – γ transition [31], [32], [38], [39],

[43], [45]. Overall, two main peaks associated to the γ mode can be seen: their duration is a few microseconds and their amplitude is only slightly modulated by the RF voltage. When the amplitude of the RF voltage is much lower than the one of the LF voltage, giving the much slower oscillation of the LF voltage waveform, many ions accumulate on the cathode side. This leads to a more intense electric field intensity close to the cathode and thus a more intense population of high-energy electrons in this region. In atmospheric-pressure plasmas characterized by low electron energy transport lengths, the energy gained by the electrons in the high electric field regions thus becomes redistributed locally [52], [53]. Therefore, these high-energy electrons can locally contribute to the population of Ar excited states, giving rise to more prominent Ar metastable densities close to the cathode seen in the experiments.

In the signal recorded at the top electrode, in black in Figure 3, a strong dissymmetry on the amplitude is observed. This confirms that the maximum population of Ar($1s_3$) states occurs when the discharge is in the γ mode characterized by significant electron heating and electron energy dissipation through collisions in the cathode fall and thus significant production of Ar metastable atoms in this region through electron-neutral excitation collisions [38], [47]. On the contrary, in the center of the gap, in red in Figure 3 the two peaks of Ar($1s_3$) densities have almost the same amplitude. In fact, the excess electrons created by the electron avalanches during the γ mode in the sheath must be evacuated to maintain the quasi neutrality in the bulk. Hence, the electric field must deform to allow electrons to cross the gap from cathode to anode. This deformation is accompanied by an increase of the electron temperature all along de discharge gap, creating the γ signature not only in the sheath but also in the bulk. This aspect is further confirmed below in the simulations of the electron temperature. In the present 50 kHz – 5 MHz DBD, a typical RF-α mode, characterized by very low populations of high-energy electrons, and thus very low production rates of Ar metastable atoms [38], [47], occurs in between the γ phases [13], [29], [44].

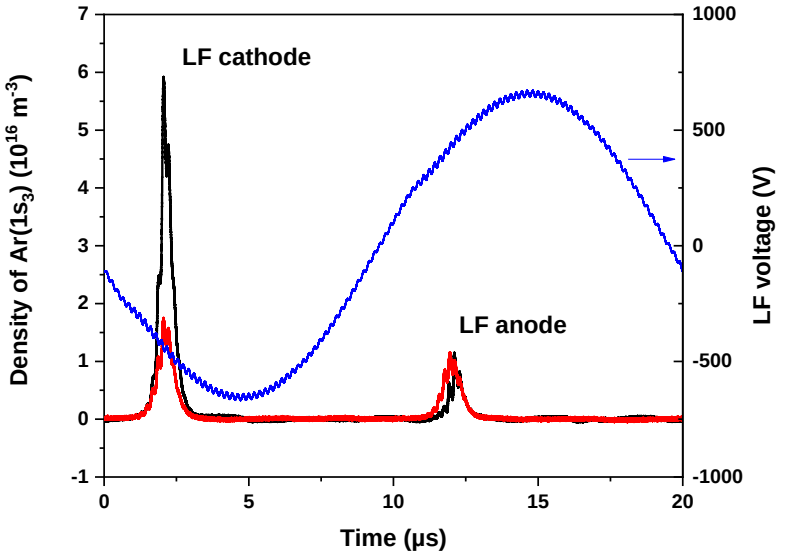

FIGURE 3. TIME VARIATION OF THE NUMBER DENSITY OF AR($1s_3$) ATOMS, CLOSE TO THE TOP ELECTRODE (IN BLACK), AND IN THE CENTER (IN RED) DURING A LF PERIOD; V_{LF} = 650 V, V_{RF}= 195 V; THE LF VOLTAGE IS APPLIED AT THE TOP ELECTRODE (IN BLUE)

Ar($1s_3$) metastable atoms are also measured near the top electrode for different amplitudes of the RF voltage between 0 (LF 650 V only) and 290 V (LF 650 V and RF 290 V). The results are shown in Figure 4 during the half-period of the applied LF voltage in which the γ mode appears at the top electrode (same dissymmetry as in Figure 3 is observed for the other half-period, not shown in Figure 4). Again, the main peak corresponds to the γ mode [47]. With the increase in amplitude of the RF voltage, temporal modulation over the RF cycle appears. In addition, the maximum value of the number density of Ar($1s_3$) states decreases, and the main peak occurs earlier during the LF cycle, i.e. for a lower value of the applied LF voltage amplitude. Furthermore, the full width at half maximum of the main peak decreases; this result suggests that the γ breakdown lasts longer when the amplitude of the RF voltage increases.

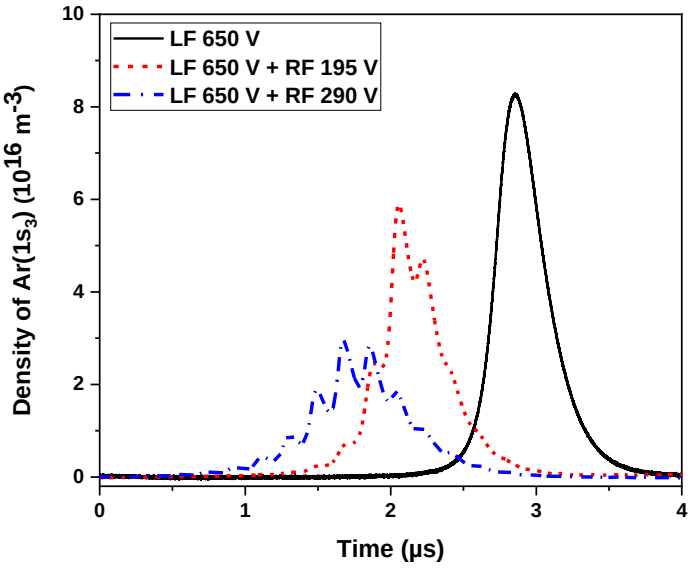

FIGURE 4. NUMBER DENSITY OF AR($1s_3$) ATOMS RECORDED CLOSE TO THE TOP ELECTRODE OVER HALF-CYCLE OF THE APPLIED LF VOLTAGE FOR DIFFERENT AMPLITUDES OF THE RF VOLTAGE.

3.2. Analysis of the Ar $2p_1 \rightarrow 1s_2$ line emission intensity

In Ar-based DBD, optical emission spectra show several lines linked to Ar $2p_x \rightarrow 1s_y$ transitions [40]. One of the most important ones occurs at 750.4 nm (Ar $2p_1 \rightarrow 1s_2$). Considering that the Ar $2p_1$ state, at 13.48 eV, is essentially populated by the electron-impact excitation from the ground-state Ar atoms [54], [55], one can conclude that the 750.4 nm line emission intensity characterizes the presence of high-energy electrons. Figure 5 (a)-(c) show the space- and time-resolved mapping of the 750.4 nm line emission intensity during a half-period of the LF signal for the same experimental conditions as in Figure 4. As observed in previous studies of low-frequency DBDs operated in the homogeneous regime [49], [56], [57], the case of LF 650 V and RF 0 V (Figure 5 (a)) reveals a single peak per half cycle of the applied LF voltage, with a maximum value in the cathode fall. In line with the prominent excitation pathway of the Ar $2p_1$ state, the drastic increase of the 750.4 nm line emission intensity in the sheath reveals a significant rise in the population of high-energy electrons in this region. Similar results can be seen in dual-frequency DBD (Figure 5 (b) and Figure 5 (c)), with

larger emission intensities in the γ mode than in the RF-α mode [38]. Despite the increase of the RF voltage from 195 to 290 V, Figure 5 (b) and Figure 5 (c) show no significant 750.4 nm emission outside the γ regime. In the case of LF 650 V and RF 195 V, it can be seen in Figure 5 (b) that the discharge is in the γ mode between about 1 and 2.5 μs, and it is in the α mode during the rest of the LF cycle. During the γ regime, the 750.4 nm line emission intensity oscillates with the RF voltage. Furthermore, the intensity first increases at about 500 μm from the cathode, and then gets closer to the cathode during the four following RF cycles. When the Ar $2p_1 \rightarrow 1s_2$ emission reaches a maximum value, it is at about 100 μm from the cathode. The variation of the position of the emission maximum is most likely related to the contraction of the cathode fall occurring with the γ breakdown. During this breakdown, the emission propagates throughout the gap with a decreasing amplitude up to about 300 μm from the anode where it begins to slightly increase. Similar behavior can be seen in Figure 5 (c) for LF 650 V and RF 290 V, with the γ mode occurring earlier during the LF cycle for RF 290 V than for RF 195 V, and being longer. Figure 5 (d) presents the effects of the amplitude of the RF voltage on the 750.4 nm line emission intensity recorded close to the cathode (around 1.75 mm from the bottom electrode, where it reaches a maximum value). Clearly, the 750.4 nm emission decreases with the rise of the RF voltage amplitude. In addition, the temporal width of the Ar $2p_1 \rightarrow 1s_2$ emission is larger when the amplitude of the RF voltage is higher. These results match the ones presented in Figure 4 for Ar($1s_3$) states; we will come back to this point later.

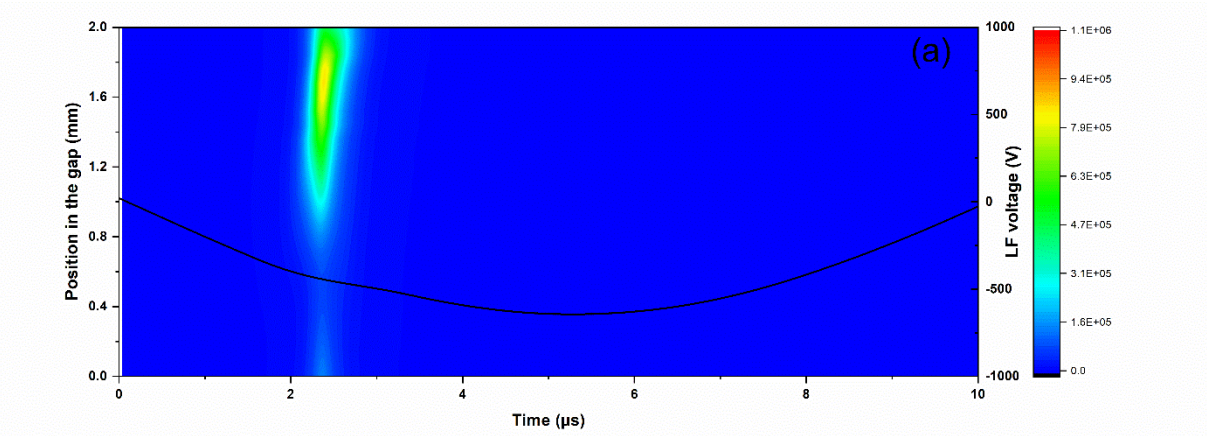
(a)
Position in the gap (mm)
Time (μs)
LF voltage (V)
2.0
1.6
1.2
0.8
0.4
0.0
0
2
4
6
8
10
1000
500
0
-500
-1000
1.1E+06
9.4E+05
7.9E+05
6.3E+05
4.7E+05
3.1E+05
1.6E+05
0.0

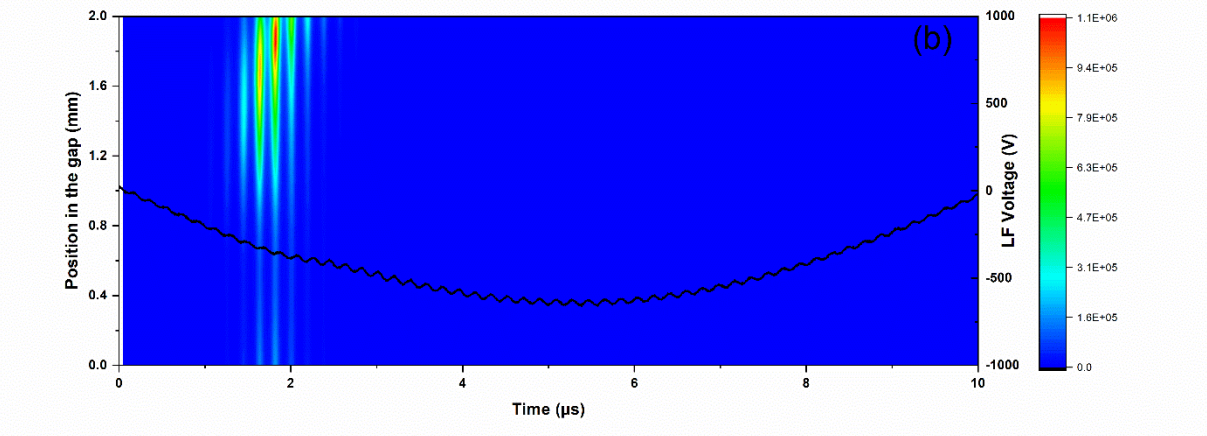
(b)
Position in the gap (mm)
Time (μs)
LF Voltage (V)
2.0
1.6
1.2
0.8
0.4
0.0
0
2
4
6
8
10
1000
500
0
-500
-1000
1.1E+06
9.4E+05
7.9E+05
6.3E+05
4.7E+05
3.1E+05
1.6E+05
0.0

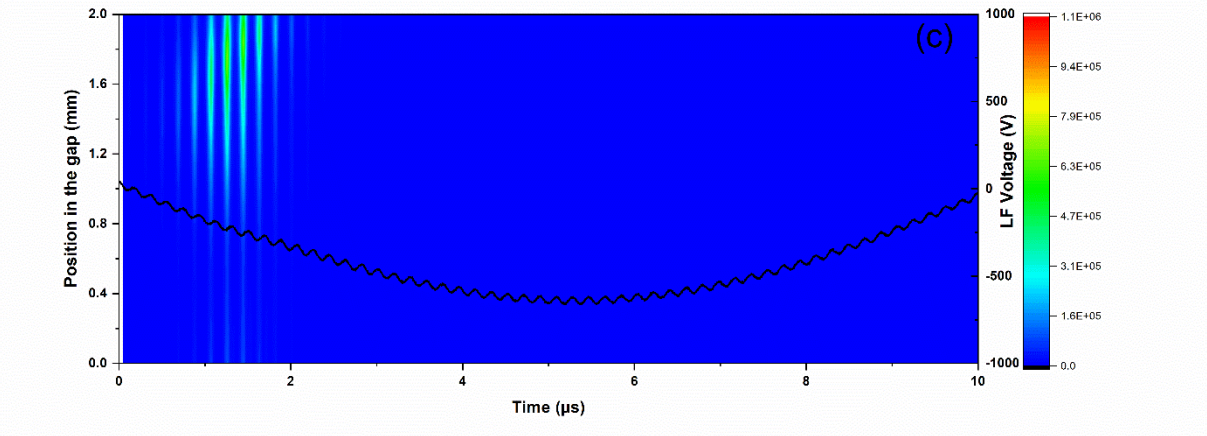
(c)
Position in the gap (mm)
Time (μs)
LF Voltage (V)
2.0
1.6
1.2
0.8
0.4
0.0
0
2
4
6
8
10
1000
500
0
-500
-1000
1.1E+06
9.4E+05
7.9E+05
6.3E+05
4.7E+05
3.1E+05
1.6E+05
0.0

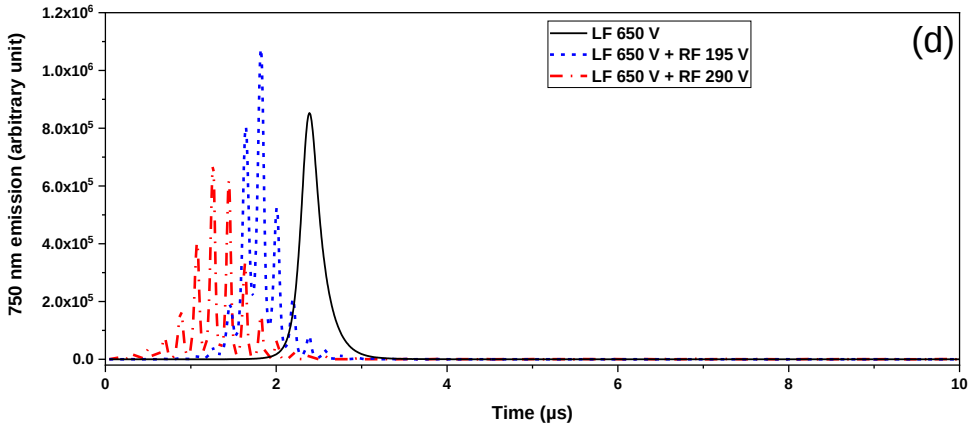

FIGURE 5. SPACE- AND TIME-RESOLVED MAPPING OF THE AR 750.4 NM LINE EMISSION INTENSITY RECORDED IN THE DUAL-FREQUENCY AR-BASED DBD FOR DIFFERENT AMPLITUDES OF THE RF VOLTAGE: (A)LF 650 V; RF 0 V, (B) LF 650 V, RF 195 V, AND (C) LF 650 V; RF 290 V. IN ALL SPATIO-TEMPORAL MAPPINGS, THE RESULTS ARE SHOWN FOR HALF-CYCLE OF THE APPLIED LF VOLTAGE, WITH THE TOP ELECTRODE BEING THE LF CATHODE AND THE LOWER ONE BEING THE LF ANODE. IN (D), THE TEMPORAL PROFILE OF THE AR 750.4 NM EMISSION RECORDED CLOSE TO THE CATHODE (AT AROUND 1.75 MM I.E. 0.25 MM FROM THE CATHODE) ARE SHOWN FOR RF 0 V, RF 195 V, AND RF 290 V.

3.3. Analysis of the continuum emission intensity

In Ar-based DBDs sustained by RF excitation, in addition to the Ar $2p_x \rightarrow 1s_y$ transitions, optical emission spectra typically show significant continuum emission between 300 and 650 nm [58]. The origin of this continuum in Ar-NH_3 DBD is not fully determined. However, in weakly-ionized plasmas, it is usually attributed to electron-atom neutral Bremsstrahlung [28], [39], [59]. At a fixed pressure (and thus at a fixed population of neutral atoms), this implies that the continuum emission intensity is related to the electron number density and to the electron average energy (or electron temperature, assuming Maxwellian energy distribution function) [60]. This is in agreement with the fact that it is commonly observed in RF DBD and not in low-frequency DBD characterized by much lower time-averaged electron populations [53]. Furthermore, in RF DBDs, the RF voltage amplitude (or RF power amplitude) has little impact on the electron temperature [28], as confirmed later using the 1D fluid model. Therefore, over the range of experimental conditions investigated, it can be assumed that variations in continuum emission intensity as RF voltage is varied are related to

variations in electron densities. Hence, in Ar-based DBD, the 750.4 nm emission mostly probes the population of high-energy electrons, whereas the continuum emission predominantly describes the total number density of electrons [58], [61]. The spatio-temporal mapping of the continuum emission is also analyzed in the dual-frequency DBD. Here, to avoid perturbation by other emission from Ar $2p_x \rightarrow 1s_y$ transitions, measurements are made at 500 nm.

Figure 6 (a)-(b) show the space- and time-resolved mapping of the 500 nm continuum emission intensity during a half-period of the LF signal for the same experimental conditions as in Figure 5. Here, the case of LF 650 V and RF 0 V is not shown since no continuum was observed. Clearly, the 500 nm emission presented in Figure 6 (a) (LF 650 V and RF 195 V) and Figure 6 (b) (LF 650 V and RF 290 V) behaves quite differently than the emission at 750.4 nm shown in Figure 5 (b) and Figure 5 (c) for the same experimental conditions. First, the continuum emission is present in both γ mode (as for the 750.4 nm emission) and RF-α mode (no emission at 750.4 nm). In both cases, the intensity is RF modulated. Second, the continuum emission appears in the bulk, with maximum intensity occurring towards the LF anode (it is maximum close to the cathode at 750.4 nm). Third, the maxima of the continuum intensity are temporally delayed by about 30 ns with respect to the one at 750.4 nm; such behavior results from the lifetime of Ar($2p_1$) state (22 ns) which would delay the argon emission. As mentioned above, the continuum emission being linked to the electron number density, the signal at 500 nm appears when and where the electron population is high, i.e. in the plasma bulk during the γ breakdown and in the RF-α regime. As for the position of the plasma bulk in the gap, it depends on the one of the cathode fall. On one hand, when γ breakdown in the cathode sheath occurs, the bulk is closest to the anode and the continuum emission is more prominent in this region, as seen in Figure 6 (a) and Figure 6 (b). On the other hand, in the RF-α regime, the discharge is centered between the two electrodes and the continuum emission appears near the center of the gap.

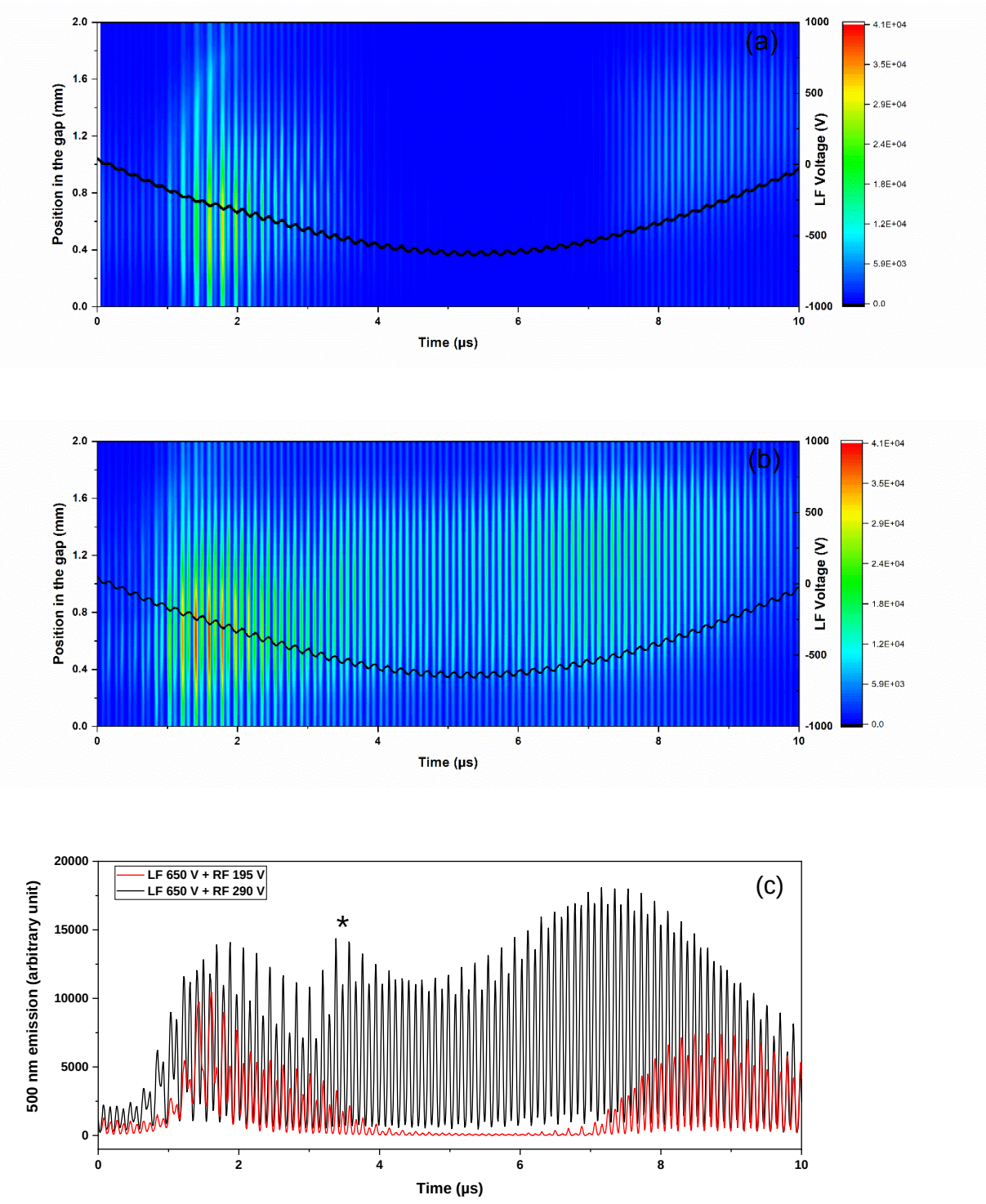

FIGURE 6. SPACE- AND TIME-RESOLVED MAPPING OF THE 500 NM CONTINUUM EMISSION INTENSITY RECORDED IN THE DUAL-FREQUENCY AR-BASED DBD FOR DIFFERENT AMPLITUDES OF THE RF VOLTAGE: (A) LF 650 V, RF 195 V AND (B) LF 650V; RF 290 V. IN BOTH SPATIO-TEMPORAL MAPPINGS, THE RESULTS ARE SHOWN FOR HALF-CYCLE OF THE APPLIED LF VOLTAGE, WITH THE TOP ELECTRODE BEING THE LF CATHODE AND THE LOWER ONE BEING THE LF ANODE. IN (C), THE TEMPORAL PROFILE OF THE AR 500 NM EMISSION RECORDED CLOSE TO THE CATHODE (AT 1.44 MM I.E. 0.56 MM FROM THE ANODE) ARE SHOWN FOR RF 195 V AND RF 290 V.

In line with the results presented in Figure 5 (d) for the 750.4 nm emission, Figure 6 (c) shows the effects of the RF voltage amplitude on the continuum emission intensity recorded close to the cathode (at 1.44 mm). When the amplitude of the RF voltage increases from 190 to 290 V, the continuum emission intensity rises significantly in the RF-α mode, which a much less prominent increase in the γ mode. Between the γ and RF-α modes (between 3 and 7 µs), Figure 6 (c) reveals that the continuum emission intensity strongly depends on the amplitude of the RF voltage. In contrast, the time domain between the RF-α and γ regimes (between 0 and 1 µs) remains very little emissive for both RF 195 V and RF 290 V. Finally, it is worth highlighting that for V_{RF}=290 V, an additional peak appears around 3.5 µs (labeled with a star in Figure 6 (c)). The origin of this peak will be defined later with the understanding of the time variation of the gas voltage.

4. 1D FLUID MODELING AND DISCUSSION

As shown in the previous section, the RF voltage amplitude has different effects on the number density of Ar($1s_3$) atoms, measured at two positions in the gas gap (see Figure 3 and Figure 4), on the population of high-energy electrons, deduced from the Ar 750.4 nm line emission intensity (see Figure 5), and on the total number density of electrons, deduced from the intensity of the continuum emission (see Figure 6). On one hand, similar findings are obtained from the measurements of Ar($1s_3$) number densities and 750.4 nm line emission intensity; this results from the fact that Ar($1s_3$) and Ar($2p_1$) levels are mostly populated by electron-impact excitation from the ground state Ar atoms (requiring 11.71, and 13.48 eV for Ar($1s_3$) and Ar($2p_1$), respectively) and their excitation rates therefore reflect the population of high-energy electrons. In both sets of data, the maximum values observed in the γ mode: (i) decrease with the rise of the RF voltage amplitude, (ii) appear earlier in the LF cycle for RF 290 V than for RF 195 V, and (iii) last for a longer time with the rise of the RF voltage amplitude. On the other hand, the continuum emission observed in the bulk, which is related

to the number density of electrons, increases significantly between RF 195 V and RF 290 V, with a more prominent rise in the RF-α mode than in the γ regime.

Additional information can be obtained by comparing the space- and time-resolved optical data recorded in this study with the predictions of a 1D fluid model of Ar-based DBD described and validated in a previous work [47]. This model solves the continuity and momentum equations for all species and the energy equation for electrons. It considers 7 species (Ar, Ar^+, Ar_2^+, Ar(1s), Ar_2*, photons and e^-) through 11 reactions. Secondary electron emission from dielectric surfaces, induced by impinging of Ar^+, Ar_2^+, Ar(1s), Ar_2* and VUV photons is also considered. All details on reaction rates and secondary electron emission coefficients are provided in [47]. Of note, Ar has four Ar(1s) levels: Ar($1s_2$), Ar($1s_3$), Ar($1s_4$), and Ar($1s_5$), of which Ar($1s_3$) and Ar($1s_5$) are long-lived metastable states. But due to the resonance radiation trapping of $1s_2 \rightarrow {}^1S_0$ and $1s_4 \rightarrow {}^1S_0$ photons, where ${}^1S_0$ is the Ar ground state, the effective lifetimes of the resonance states Ar($1s_2$) and Ar($1s_4$) become comparable to those of metastable states. Hence, these four states can be considered to be close to their statistical equilibrium, with number density ratios 3:1:3:5 for Ar($1s_2$):Ar($1s_3$):Ar($1s_4$):Ar($1s_5$) states, respectively [49], [62]. Under this assumption, these four states are treated as a single Ar(1s) state, with a total density 12 times higher than the measured density of the Ar($1s_3$) level [47].

As indicated before, experiments are done for a LF voltage amplitude of 650 V, which is 50 V above the LF breakdown for the investigated experimental conditions. In line with this result, calculations are done at V_{LF}=940 V, a value 50 V above the lower LF voltage allowing a LF discharge breakdown in the model. As for the RF voltage amplitude, the first value is set at the lowest value allowing to get a single frequency RF discharge, V_{RF}=350 V. As for the second V_{RF} value, in line with the experiments, it is fixed 100 V above this value, at 450 V. Here, the differences between the experimental and simulated values of the LF and RF breakdown voltages can be partially attributed to the error on the

dielectric permittivity of the Al_2O_3 dielectrics placed on top of the metallic electrodes. This permittivity is not measured and is set at 9 in the model [38]. Despite such slight differences in the amplitudes of LF and RF voltages between the simulations and experiment, the agreements are relatively good, as demonstrated below.

Figure 7 shows the Ar(1s) number densities obtained from the model for the two RF voltage amplitudes. In line with the time-resolved tunable diode laser absorption spectroscopy measurements recorded at two positions in the gas gap (Figure 3), the spatio-temporal mappings displayed in Figure 7 (a) (LF 950 V, RF 350 V) and Figure 7 (b) (LF 950 V, RF 450 V) reveal a significant rise only once per half-period of the applied LF voltage. In addition, such increase appears mostly in the cathode fall in the γ mode. Absolute values of Ar($1s_3$) states predicted by the model (calculated Ar(1s) density divided by 12) are also comparable to the ones recorded experimentally (for V_{RF}=290 V, measured Ar($1s_3$) density is $5.9*10^{16}$ m^{-3}, calculated Ar($1s_3$) density is $1.4*10^{17}$ m^{-3}). As in the experiment (Figure 3), a small increase is also observed in Figure 7 (a) and Figure 7 (b) close to the anode. Of note, the ratio of the maximum at the cathode and the anode is about 5.3 in the calculations and 5.2 in the experiments for the low RF voltage value. At the higher RF voltage, this ratio is 4.8 in the calculations and 4.3 in the model. As for the evolution between RF 350 V and RF 450 V of the Ar(1s) maximum number density integrated over the top 500 µm of the gap near the top electrode, it also follows the same trend as the ones observed experimentally (Figure 4). In particular, the maximum density decreases by 27% following the increase of the RF voltage amplitude by 100 V. These results could be explained by a decrease of the quantity of high-energy electrons when the RF voltage amplitude increases [35]. In addition, the peak density of Ar(1s) atoms appears earlier on the LF cycle (this means for a lower amplitude of the LF voltage), and broadens between RF 350 V and RF 450 V. As shown in Figure 7 (a) and Figure 7 (b), the Ar(1s) population also increases close to the anode, as observed in the experiments (Figure 3).

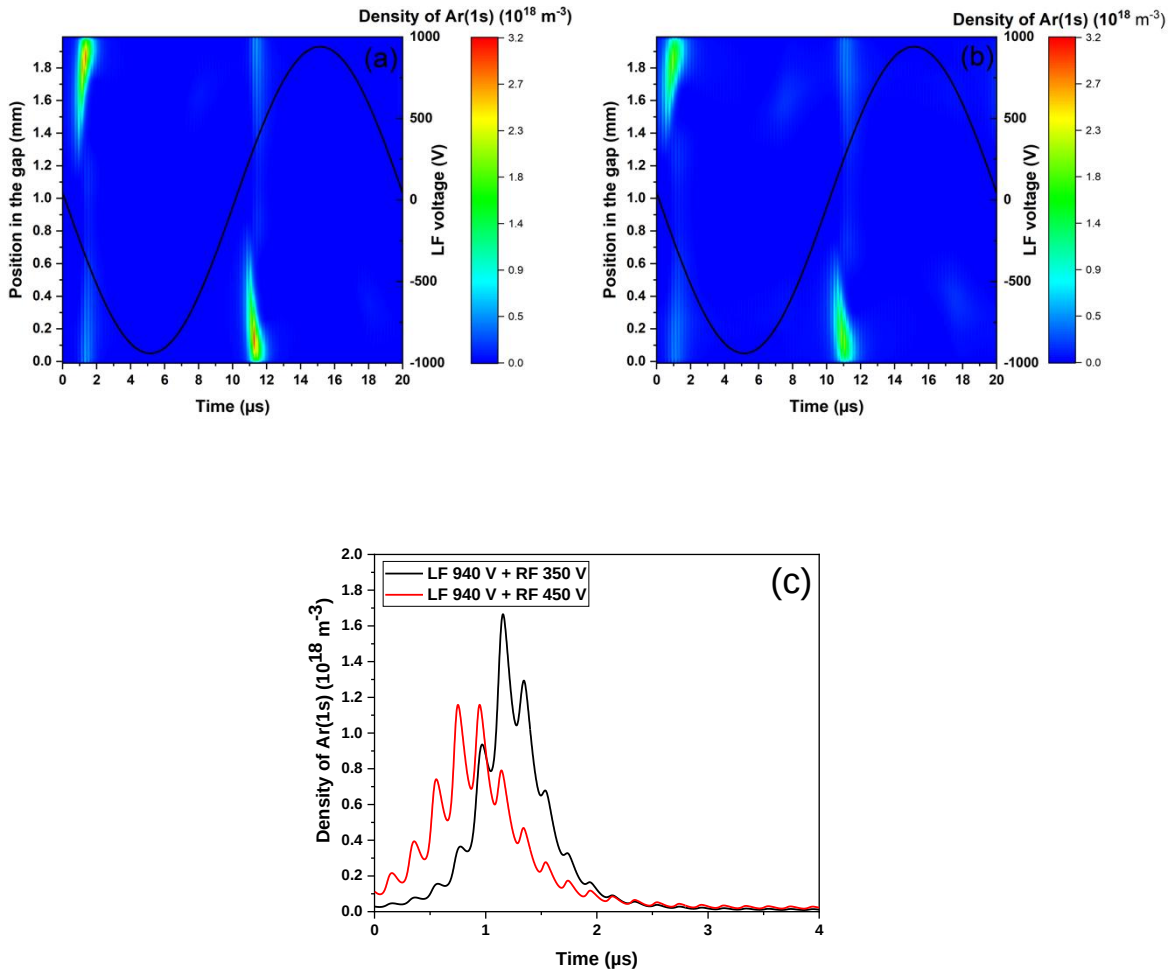

FIGURE 7. CALCULATED VALUES OF THE AR(1S) NUMBER DENSITY IN THE GAP AS FUNCTION OF TIME FOR : (A) LF 940 V AND RF 350 V, (B) LF 940 V AND RF 450 V. IN (C), CALCULATED AR(1S) NUMBER DENSITY VALUES INTEGRATED OVER THE TOP 500 μM OF THE GAP NEAR THE TOP ELECTRODE (THE CATHODE) BETWEEN 0 AND 4 μS.

Following such validation, the space- and time-resolved optical measurements are further analyzed based on calculated values of n_e (electron number density), n_i (positive ion number density) and T_e (electron temperature). Figure 8 presents spatio-temporal mappings of n_e, n_i and T_e obtained from the model [47] during a LF cycle for the two RF voltage amplitudes. In both, Figure 8 (a) (LF 950 V, RF 350 V) and Figure 8 (b) (LF 950 V, RF 450 V), n_e is high in the bulk and low close to the walls; this defines the sheath region. In addition, there is a local rise close to the anode in the electron density near the γ breakdown. Between RF 350 V and RF 450 V, there is an overall increase in the electron

density, with most of this increase occurring in the RF-α regime. Overall, the space- and time averaged value of n_e rises by 31%. Assuming that the emission at 500 nm is attributed to the electron-atom neutral Bremsstrahlung [28], [39], and is thus mostly linked to n_e (assuming only small variations of T_e, as confirmed below), the increase of n_e deduced from the model in Figure 8 (a) and Figure 8 (b) is consistent with the one seeing in the experiment in Figure 6 (the time and space-integrated continuum emission intensity increases by about factor 2 between RF 195 V and RF 290 V).

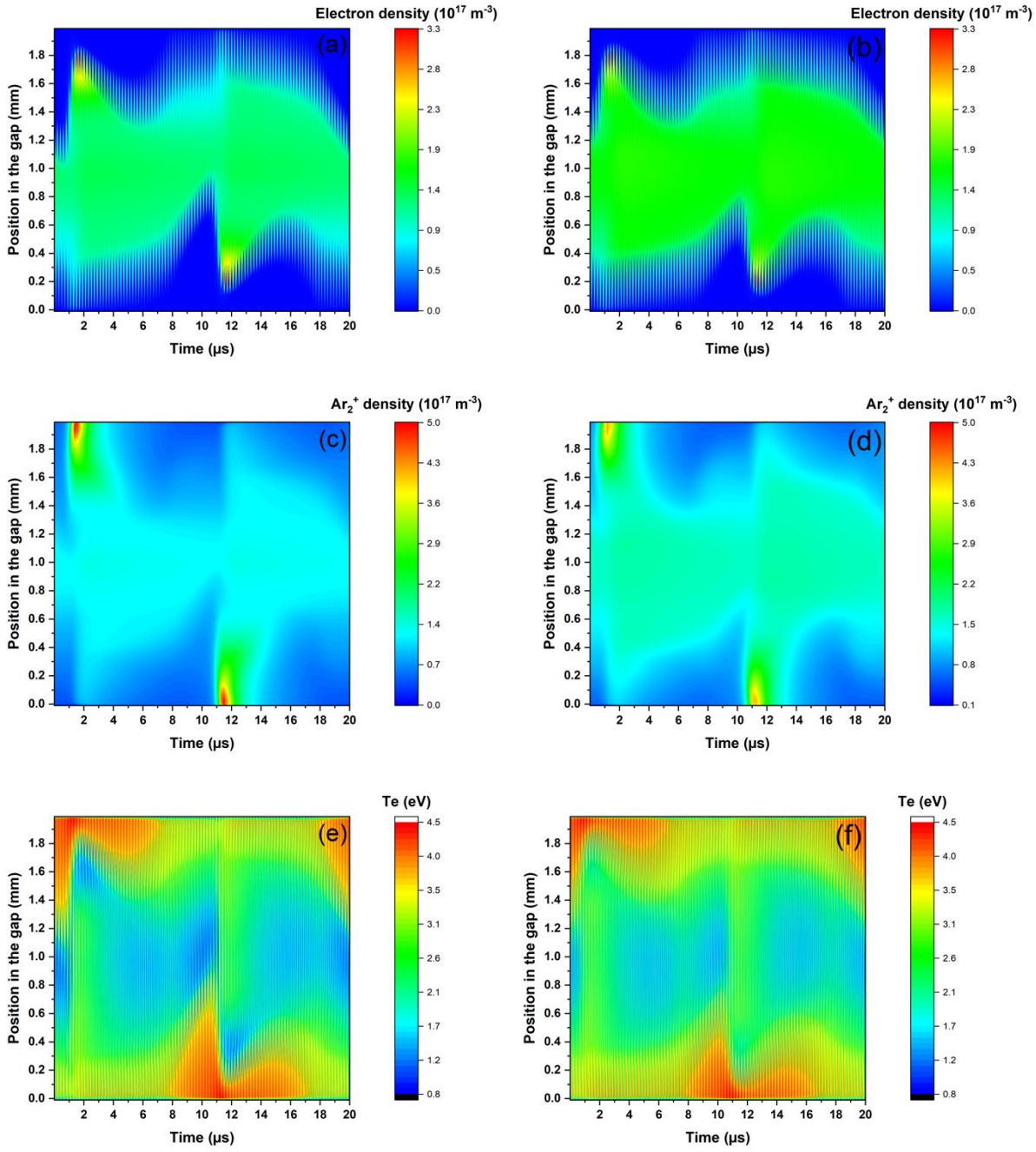

FIGURE 8. VALUES OF THE ELECTRON DENSITY (A,B), POSITIVE ION DENSITY (C,D), AND ELECTRON TEMPERATURE (E,F) OBTAINED FROM THE MODEL IN THE GAP AS FUNCTION OF TIME FOR : (A,C,E) LF 940 V AND RF 350 V, (B,D,F) LF 940 V AND RF 450 V.

Figure 8 (c) and Figure 8 (d) show the spatio-temporal evolution of the Ar_2^+ ions density following the increase of the RF voltage amplitude. In both conditions, the Ar_2^+ density is higher in the bulk than in the sheaths, except during the γ breakdown. In addition, the temporal evolution of the ions is slow at

the RF scale: in contrast to the electron density that evolves at both RF and LF time scales, the population of Ar_2^+ mostly "sees" the LF voltage. Since ionization of Ar by high energy electrons produces Ar^+, which is rapidly converted to Ar_2^+ ions by 3-body reactions with 2 ground-state Ar atoms [47], Ar_2^+ is the dominant positive ion and, at the LF scale, its behavior is expected to follow the one of the high-energy electron population (behavior visible in both the number density of Ar(1s) atoms (Figure 4) and the Ar 750.4 nm line emission intensity (Figure 5)). Here, the space- and time-averaged value of Ar_2^+ increases by 24% between RF 350 V and RF 450 V.

As for the spatio-temporal mapping of the electron temperature presented in Figure 8 (e) and Figure 8 (f), the values are lower in the bulk than in the sheath. As expected, the maxima of T_e appear in the cathode sheath during γ breakdown. At the α - γ transition, one can also see an increase of T_e throughout the gap: this is the consequence of the deformation of electric field in the bulk to evacuate the electrons created in the cathodic sheath in order to maintain the quasi-neutrality in the plasma bulk. Such behavior corroborates the increase from the cathode to the anode observed during γ breakdown in Figure 4 for the Ar(1s) and in Figure 5 for the Ar 750.4 nm line emission intensity. Figure 8 (e) and Figure 8 (f) further show that the space- and time-averaged value of T_e only slightly rises (+5%) between RF 350 V and RF 450 V. Here, this very small increase mostly results from an increase of T_e in the bulk, which is partially compensated by a decrease in the spatio-temporal domain of high T_e values in the γ regime (the cathode sheath is much larger at RF 350 V than at RF 450 V). Such aspect is investigated in more details by examining the behavior of the gas voltage. Here, it is worth recalling that in DBDs, due to the presence of charges on dielectric surfaces, the voltage applied to the gas does not correspond to the voltage applied to the electrodes by the LF and RF generators [63].

Figure 9 (a) and Figure 9 (b) show the gas voltage calculated from the model for the two RF voltage amplitudes. In both cases, the shape is characteristic of a low-frequency DBD operated in a glow regime [64] to which is added a RF voltage. The γ breakdown is recognizable by the fast drop in the gas voltage amplitude just after its maximum value. The RF-α regime occurs between two γ breakdowns, when the gas voltage oscillates around 0 V, i.e. when the LF contribution to the gas voltage is low. As expected, the RF-α mode is directly linked to the amplitude of the RF voltage: thus, by increasing the RF voltage amplitude, events due to the α regime are reinforced. For the γ mode, Figure 9 (a) and Figure 9 (b) show that the trend is different. The increase from RF 350 V to RF 450 V globally increases n_e and n_i in the bulk, as seen in Figure 8, and this promotes LF breakdown in the γ mode. Here, γ breakdown occurs at a lower gas voltage with increasing RF voltage amplitude (maximum gas voltage is 844 V for the LF + RF 350 V and 787 V for the LF + RF 450 V).

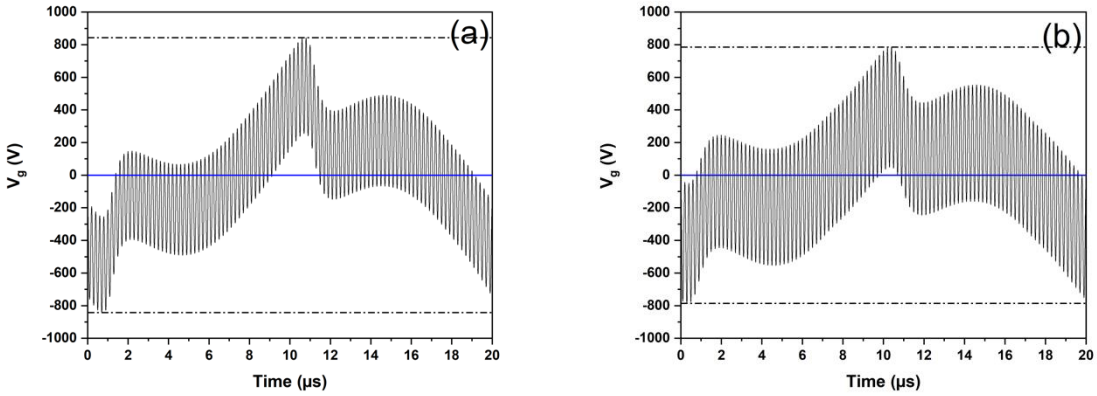

FIGURE 9. CALCULATION OF THE GAS VOLTAGE DURING THE LF PERIOD FOR (A) LF 940 V AND RF 350 V, (B) LF 940 V AND RF 450 V.

Figure 10 presents a decomposition between LF (a) and RF (b) contributions of the voltage applied to the gas and the voltage across the dielectrics (V_{ds}) for the same conditions as in Figure 9. Here, the LF contribution corresponds to the RF-smoothed signals of V_g and V_{ds} and the RF contribution corresponds to the amplitude of the RF oscillations on V_g and V_{ds}, calculated from the difference between their upper and lower envelope values. For both RF 350 V and RF 450 V, Figure 10 (a)

reveals that the LF gas voltage increases until the γ breakdown, after which it decreases during a short time. The second rise of V_g starts around 2 and 12 µs: this results from the fact that after the γ breakdown, the applied LF voltage is still rising such that V_g follows the same trend. This latter behavior, coupled with the fact that for the LF 940 V + RF 450 V, n_e is greater than for LF 940 V + RF 350 V, also explains the origin of the additional peak of the continuum emission during the γ-to-α transition displayed in Figure 6 (c). By increasing the RF voltage, the γ breakdown appears earlier, i.e. for a lower LF voltage amplitude. In addition, the slope of decrease/increase of V_g due to dielectric charge after the γ breakdown is lower for LF 940 V + RF 450 V, than for LF 940 V + RF 350 V. Concerning V_{ds}, the main visible change is also linked to the time of the increase/decrease of V_{ds} after the γ breakdown. Since the α - γ transition occurs earlier for higher RF voltage amplitudes, i.e. for a lower LF voltage, the dielectric charges earlier and slower, and this induces the same behavior on V_{ds}. Consequently, the rise in the population of Ar(1s) and Ar(2p) is expected to occur earlier and both peaks are expected to broaden when the RF voltage amplitude rises; such findings are consistent with the experimental results presented in Figure 4 and Figure 5.

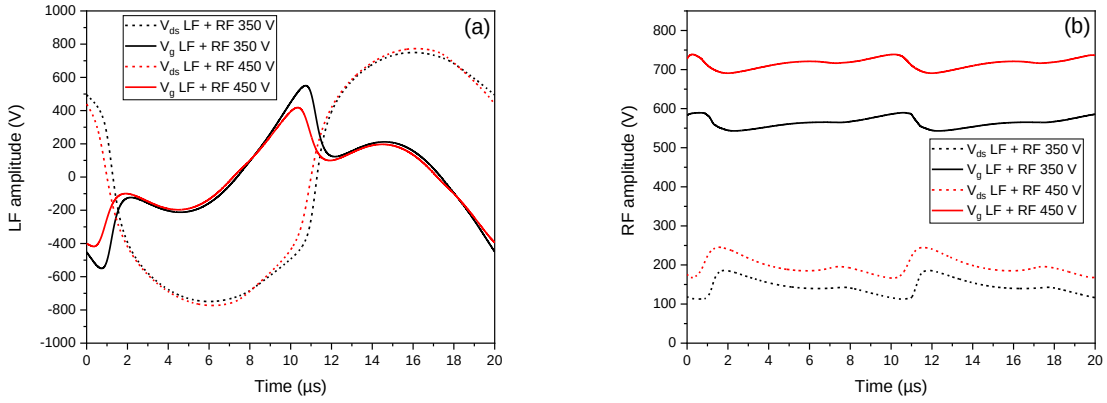

FIGURE 10. (A) LF CONTRIBUTION TO VG AND VDS, (B) RF CONTRIBUTION TO VG AND VDS, OBTAINED FROM THE MODEL (LF 940 V AND RF 350 V IN BLACK, LF 940 V AND RF 450 V IN RED).

As for the RF amplitude, Figure 10 (b), reveals that most of the applied RF voltage is applied to the gas, with only a small drop across dielectrics. When the γ breakdown occurs, charge density increases in the plasma (particularly in the sheath) such that losses and thus charging at the dielectric walls also increase. With such charging of dielectrics, V_{ds} increases, and this leads to a decrease of V_g. Over the range of experimental conditions investigated, Figure 10 (b) further shows that the amplitude of the RF component of V_g increases by only 75 V (averaged over the LF cycle) following the increase between RF 350 V to RF 450 V. Hence, a larger fraction of the applied voltage goes to the dielectrics with increasing amplitude of the RF voltage.

Such analysis of V_g and V_{ds} clearly underlines the importance of dielectrics for a detailed analysis of DBDs exhibiting the α - γ transition. On one hand, as the amplitude of the RF voltage increases, the γ breakdown appears earlier in the LF cycle, a lower maximum gas voltage is distributed in the gap (mainly in the cathode sheath) and this yields to a weaker local electric field. This weaker local electric field accelerates less the electrons in the sheath, inducing a decrease of the spatial and temporal domains of high energy electrons. This results in a decrease in the local production rates of reactions requiring high-energy electrons, for example, excitation and ionization of Ar in the cathode sheath edge. Again, this finding is consistent with the results presented in Figure 4 and Figure 5 showing a decrease of the main Ar(1s) and Ar(2p) peak intensities when V_{RF} is increased from 195 V to 290 V. On the other hand, a rise in the amplitude of the RF voltage increases the power absorbed and dissipated by electrons in the RF-α mode. In line with the spatio-temporal mappings of the continuum emission displayed in Figure 6, this produces higher number densities of charged species in the bulk, which explains the α - γ transition for a lower gas voltage value.

5. Conclusion

Spatio-temporal mappings of the populations of metastable atoms Ar(1s) and of the emission intensities of Ar(2p) states as well as the continuum emission in Ar-based DBDs exhibiting the α - γ transition were analyzed by space- and time-resolved optical absorption and emission spectroscopy. It was shown that the 50 kHz–5 MHz dual-frequency discharge allows to control the discharge fundamental properties through judicious change of the amplitude of the RF voltage. The higher is the RF voltage amplitude, the higher is the electron density in the bulk and the closer the discharge is to the typical RF-α regime characterized by an ohmic heating of plasma electrons in the bulk. Consequently, in such conditions, the phenomena linked to the γ breakdown (in particular, the production of high-energy electrons in the cathode sheath) have a much lower contribution. It was further shown that increasing the RF voltage amplitude reduces and delays the excitation rate of Ar atoms, thus the maximum values of the Ar(1s) metastable density and of the Ar 750.4 nm line emission intensity, observed in the γ mode. On the other hand, the continuum emission observed in the bulk, which is related to the number density of electrons, increased significantly, with a more prominent rise in the RF-α mode than in the γ regime. Such behaviors, which seemed surprising at first glance, are very well explained by the decrease in the gas voltage necessary to cause the self-maintenance of the cathode sheath when the electrons and ions densities increase, and leads therefore to the γ breakdown.

6. Acknowledgments

The work carried out in France was supported by the Agence Nationale de la Recherche through the Investissement d'avenir program (ANR10LABX2201). As for the one done in Canada, it was funded by the National Science and Engineering Research Council (NSERC RGPIN-2018-04550) and by the Fondation Courtois. The 'Réseau des Plasmas Froids' of CNRS/MCRT (France) is acknowledged for

providing the DFB diode laser and the travel support for Nader Sadeghi and LPGP, Orsay (France) for lending the MCS6A Multiscaler. All authors would like to acknowledge the financial support of the CNRS and Université de Montréal through their contributions to the International Research Network on Controlled Multifunctional Nanomaterials.

7. Data availability statement

The data that support the findings of this study are available upon request from the authors.

8. References

[1] G. M. Allen and D. M. Coleman, "Characterization of a Dual Inductively Coupled Plasma Atomic Emission Source," *Appl. Spectrosc.*, vol. 41, no. 3, pp. 381–387, 1987.

[2] J. E. Klemberg-Sapieha, O. M. Kuttel, L. Martinu, and M. R. Wertheimer, "Dual microwave-R.F. plasma deposition of functional coatings," *Thin Solid Films*, vol. 194, no. 1–2 pt 2, pp. 965–972, 1990.

[3] L. Martinu, J. E. Klemberg-Sapieha, and M. R. Wertheimer, "Dual-mode microwave/radio frequency plasma deposition of dielectric thin films," *Appl. Phys. Lett.*, vol. 54, no. 26, pp. 2645–2647, 1989.

[4] A. Raveh, L. Martinu, H. M. Hawthorne, and M. R. Wertheimer, "Mechanical and tribological properties of dual-frequency plasma-deposited diamond-like carbon," *Surf. Coatings Technol.*, vol. 58, no. 1, pp. 45–55, 1993.

[5] A. S. da Silva Sobrinho, M. Latrèche, G. Czeremuszkin, J. E. Klemberg-Sapieha, and M. R. Wertheimer, "Transparent barrier coatings on polyethylene terephthalate by single- and dual-frequency plasma-enhanced chemical vapor deposition," *J. Vac. Sci. Technol. A Vacuum, Surfaces, Film.*, vol. 16, no. 6, pp. 3190–3198, 1998.

[6] J. E. Klemberg-Sapieha, O. M. Küttel, L. Martinu, and M. R. Wertheimer, “Dual-frequency N2 and NH3 plasma modification of polyethylene and polyimide,” *J. Vac. Sci. Technol. A Vacuum, Surfaces, Film.*, vol. 9, no. 6, pp. 2975–2981, 1991.

[7] E. Kawamura, M. A. Lieberman, and D. B. Graves, “Fast 2D fluid-analytical simulation of ion energy distributions and electromagnetic effects in multi-frequency capacitive discharges,” *Plasma Sources Sci. Technol.*, vol. 23, no. 6, pp. 1–12, 2014.

[8] J. P. Booth, G. Curley, D. Marić, and P. Chabert, “Dual-frequency capacitive radiofrequency discharges: Effect of low-frequency power on electron density and ion flux,” *Plasma Sources Sci. Technol.*, vol. 19, no. 1, pp. 1–7, 2010.

[9] E. Kawamura, M. A. Lieberman, and A. J. Lichtenberg, “Stochastic heating in single and dual frequency capacitive discharges,” *Phys. Plasmas*, vol. 13, no. 5, p. 053506, 2006.

[10] T. Gans, D. O’Connell, V. Schulz-Von Der Gathen, and J. Waskoenig, “The challenge of revealing and tailoring the dynamics of radio-frequency plasmas,” *Plasma Sources Sci. Technol.*, vol. 19, no. 3, p. 034010, 2010.

[11] X. S. Li *et al.*, “Modulating effects of the low-frequency source on ion energy distributions in a dual frequency capacitively coupled plasma,” *Appl. Phys. Lett.*, vol. 93, no. 3, p. 031504, 2008.

[12] B. B. Sahu and J. G. Han, “Electron heating mode transition induced by mixing radio frequency and ultrahigh frequency dual frequency powers in capacitive discharges,” *Phys. Plasmas*, vol. 23, no. 5, pp. 1–10, 2016.

[13] M. M. Turner and P. Chabert, “Electron heating mode transitions in dual frequency capacitive discharges,” *Appl. Phys. Lett.*, vol. 89, no. 23, pp. 9–11, 2006.

[14] D. O’Connell, T. Gans, E. Semmler, and P. Awakowicz, “The role of the relative voltage and phase for frequency coupling in a dual-frequency capacitively coupled plasma,” *Appl. Phys. Lett.*, vol. 93, no. 8, pp. 1–3, 2008.

[15] W. Tsai, G. Mueller, R. Lindquist, B. Frazier, and V. Vahedi, “High selectivity plasma etching of silicon dioxide with a dual frequency 27/2 MHz capacitive radio frequency discharge,” *J. Vac. Sci. Technol. B Microelectron. Nanom. Struct.*, vol. 14, no. 5, p. 3276, 1996.

[16] V. Georgieva and A. Bogaerts, “Numerical simulation of dual frequency etching reactors: Influence of the external process parameters on the plasma characteristics,” *J. Appl. Phys.*, vol. 98, no. 2, pp. 1–13, 2005.

[17] V. Georgieva, A. Bogaerts, and R. Gijbels, “Numerical investigation of ion-energy-distribution functions in single and dual frequency capacitively coupled plasma reactors,” *Phys. Rev. E - Stat. Nonlinear, Soft Matter Phys.*, vol. 69, no. 2 2, pp. 1–11, 2004.

[18] J. Schulze, T. Gans, D. O’Connell, U. Czarnetzki, A. R. Ellingboe, and M. M. Turner, “Space and phase resolved plasma parameters in an industrial dual-frequency capacitively coupled radio-frequency discharge,” *J. Phys. D. Appl. Phys.*, vol. 40, no. 22, pp. 7008–7018, 2007.

[19] E. Semmler, P. Awakowicz, and A. Von Keudell, “Heating of a dual frequency capacitively coupled plasma via the plasma series resonance,” *Plasma Sources Sci. Technol.*, vol. 16, no. 4, pp. 839–848, 2007.

[20] P. C. Boyle, A. R. Ellingboe, and M. M. Turner, “Electrostatic modelling of dual frequency rf plasma discharges,” *Plasma Sources Sci. Technol.*, vol. 13, no. 3, pp. 493–503, 2004.

[21] P. C. Boyle, A. R. Ellingboe, and M. M. Turner, “Independent control of ion current and ion impact energy onto electrodes in dual frequency plasma devices,” *J. Phys. D. Appl. Phys.*, vol. 37, no. 5, pp. 697–701, 2004.

[22] J. K. Lee, O. V. Manuilenko, N. Y. Babaeva, H. C. Kim, and J. W. Shon, “Ion energy distribution control in single and dual frequency capacitive plasma sources,” *Plasma Sources Sci. Technol.*, vol. 14, no. 1, pp. 89–97, 2005.

[23] K. N. Kim, J. H. Lim, G. Y. Yeom, S. H. Lee, and J. K. Lee, “Effect of dual frequency on the

plasma characteristics in an internal linear inductively coupled plasma source," *Appl. Phys. Lett.*, vol. 89, no. 25, pp. 3–5, 2006.

[24] Z. Donkó and Z. L. Petrović, "Analysis of a capacitively coupled dual-frequency CF4 discharge," *Japanese J. Appl. Physics, Part 1 Regul. Pap. Short Notes Rev. Pap.*, vol. 45, no. 10 B, pp. 8151–8156, 2006.

[25] X. V. Qin, Y. H. Ting, and A. E. Wendt, "Tailored ion energy distributions at an rf-biased plasma electrode," *Plasma Sources Sci. Technol.*, vol. 19, no. 6, 2010.

[26] T. Kitajima, Y. Takeo, Z. L. Petrović, and T. Makabe, "Functional separation of biasing and sustaining voltages in two-frequency capacitively coupled plasma," *Appl. Phys. Lett.*, vol. 77, no. 4, pp. 489–491, 2000.

[27] T. H. Kim *et al.*, "Plasma characteristics of inductively coupled plasma using dual-frequency antennas," *Jpn. J. Appl. Phys.*, vol. 52, no. 5 PART 3, pp. 1–5, 2013.

[28] S. Park, W. Choe, S. Y. Moon, and J. J. Shi, "Electron Information in Single-And Dual-Frequency Capacitive Discharges at Atmospheric Pressure," *Sci. Rep.*, vol. 8, no. 1, pp. 1–10, 2018.

[29] Z. L. Zhang, J. W. M. Lim, Q. Y. Nie, X. N. Zhang, and B. H. Jiang, "Electron heating and mode transition in dual frequency atmospheric pressure argon dielectric barrier discharge," *AIP Adv.*, vol. 7, no. 10, p. 105313, 2017.

[30] Y. Liu, F. M. Elam, E. Zoethout, S. A. Starostin, M. C. M. Van De Sanden, and H. W. De Vries, "Atmospheric-pressure silica-like thin film deposition using 200 kHz/13.56 MHz dual frequency excitation," *J. Phys. D. Appl. Phys.*, vol. 52, no. 35, pp. 1–11, 2019.

[31] Y. Liu, S. A. Starostin, F. J. J. Peeters, M. C. M. Van De Sanden, and H. W. De Vries, "Atmospheric-pressure diffuse dielectric barrier discharges in Ar/O2 gas mixture using 200 kHz/13.56 MHz dual frequency excitation," *J. Phys. D. Appl. Phys.*, vol. 51, no. 11, p. 114002, 2018.

[32] F. Massines, R. Bazinette, and J. Paillol, “RF-LF dual frequency uniform dielectric barrier discharge for thin film processing,” *22nd Int. Symp. Plasma Chem.*, p. O-22-3, 2015.

[33] R. Bazinette, N. Sadeghi, and F. Massines, “Dual frequency DBD: Influence of the amplitude and the frequency of applied voltages on glow, Townsend and radiofrequency DBDs,” *Plasma Sources Sci. Technol.*, vol. 29, no. 9, p. 095010, 2020.

[34] D. B. Kim, J. K. Rhee, B. Gweon, S. Y. Moon, and W. Choe, “Comparative study of atmospheric pressure low and radio frequency microjet plasmas produced in a single electrode configuration,” *Appl. Phys. Lett.*, vol. 91, no. 15, pp. 2005–2008, 2007.

[35] F. R. Kong, Z. L. Zhang, and B. H. Jiang, “Numerical study of the discharge properties of atmospheric dielectric barrier discharge by using 200 kHz/13.56 MHz excitations,” *AIP Adv.*, vol. 8, no. 7, p. 075009, 2018.

[36] Y. Liu, F. J. J. Peeters, S. A. Starostin, M. C. M. Van De Sanden, and H. W. De Vries, “Improving uniformity of atmospheric-pressure dielectric barrier discharges using dual frequency excitation,” *Plasma Sources Sci. Technol.*, vol. 27, no. 1, pp. 1–5, 2018.

[37] Y. Liu *et al.*, “Numerical simulation of atmospheric-pressure 200 kHz/13.56 MHz dual-frequency dielectric barrier discharges,” *Plasma Sources Sci. Technol.*, vol. 27, no. 10, p. 105016, 2018.

[38] R. Magnan, G. Hagelaar, M. Chaker, and F. Massines, “Atmospheric pressure dual RF-LF frequency discharge: Influence of LF voltage amplitude on the RF discharge behavior,” *Plasma Sources Sci. Technol.*, vol. 29, no. 3, p. 035009, Feb. 2020.

[39] R. Magnan, G. Hagelaar, M. Chaker, and F. Massines, “Atmospheric pressure dual RF – LF frequency discharge : transition from α to α–γ -mode,” *Plasma Sources Sci. Technol.*, vol. 30, no. 1, p. 015010, Jan. 2021.

[40] Y. J. Zhou, Q. H. Yuan, F. Li, X. M. Wang, G. Q. Yin, and C. Z. Dong, “Nonequilibrium

atmospheric pressure plasma jet using a combination of 50 kHz/2 MHz dual-frequency power sources," *Phys. Plasmas*, vol. 20, no. 11, p. 113502, 2013.

[41] E. P. van de Ven, I.-W. Connick, and A. S. Harrus, "Advantages of dual frequency PECVD for deposition of ILD and passivation films," in *Seventh International IEEE Conference on VLSI Multilevel Interconnection*, 1990, pp. 194–201.

[42] V. Georgieva, A. Bogaerts, and R. Gijbels, "Numerical study of Ar/CF4/N2 discharges in single- and dual-frequency capacitively coupled plasma reactors," *J. Appl. Phys.*, vol. 94, no. 6, pp. 3748–3756, 2003.

[43] D. Liu, A. Yang, X. Wang, C. Chen, M. Rong, and M. G. Kong, "Electron heating and particle fluxes in dual frequency atmospheric-pressure helium capacitive discharge," *J. Phys. D. Appl. Phys.*, vol. 49, no. 49, pp. 1–7, 2016.

[44] C. Oneill, J. Waskoenig, and T. Gans, "Tailoring electron energy distribution functions through energy confinement in dual radio-frequency driven atmospheric pressure plasmas," *Appl. Phys. Lett.*, vol. 101, no. 15, pp. 1–5, 2012.

[45] J. Waskoenig and T. Gans, "Nonlinear frequency coupling in dual radio-frequency driven atmospheric pressure plasmas," *Appl. Phys. Lett.*, vol. 96, no. 18, pp. 3–6, 2010.

[46] Z. L. Zhang *et al.*, "Numerical studies of independent control of electron density and gas temperature via nonlinear coupling in dual-frequency atmospheric pressure dielectric barrier discharge plasmas," *Phys. Plasmas*, vol. 23, no. 7, p. 073501, 2016.

[47] R. Robert, G. Hagelaar, N. Sadeghi, R. Magnan, L. Stafford, and F. Massines, "Role of excimer formation and induced photoemission on the Ar metastable kinetics in atmospheric pressure Ar-NH3 dielectric barrier discharges," *Plasma Sources Sci. Technol.*, vol. 31, no. 6, p. 065010, 2022.

[48] W. L. Wiese, J. W. Brault, K. Danzmann, V. Helbig, and M. Kock, "Unified set of atomic

transition probabilities for neutral argon," *Phys. Rev. A*, vol. 39, no. 5, pp. 2461–2471, 1989.

[49] N. Sadeghi, R. Magnan, and F. Massines, "Pressure broadening of 772.376 and 772.421 nm argon lines and kinetics of argon metastable atoms," *J. Quant. Spectrosc. Radiat. Transf.*, vol. 288, p. 108264, 2022.

[50] Á. Martín Ortega, A. Lacoste, S. Béchu, A. Bès, and N. Sadeghi, "Characterization of X-ray gas attenuator plasmas by optical emission and tunable laser absorption spectroscopies," *J. Synchrotron Radiat.*, vol. 24, no. 6, pp. 1195–1208, 2017.

[51] L. Latrasse, N. Sadeghi, A. Lacoste, A. Bès, and J. Pelletier, "Characterization of high density matrix microwave argon plasmas by laser absorption and electric probe diagnostics," *J. Phys. D. Appl. Phys.*, vol. 40, no. 17, pp. 5177–5186, 2007.

[52] T. Hemke *et al.*, "Ionization by bulk heating of electrons in capacitive radio frequency atmospheric pressure microplasmas," *Plasma Sources Sci. Technol.*, vol. 22, no. 1, p. 015012, 2013.

[53] F. Massines, C. Sarra-Bournet, F. Fanelli, N. Naudé, and N. Gherardi, "Atmospheric pressure low temperature direct plasma technology: Status and challenges for thin film deposition," *Plasma Process. Polym.*, vol. 9, no. 11–12, pp. 1041–1073, 2012.

[54] J. B. Boffard, G. A. Piech, M. F. Gehrke, L. W. Anderson, and C. C. Lin, "Measurement of electron-impact excitation cross sections out of metastable levels of argon and comparison with ground-state excitation," *Phys. Rev. A - At. Mol. Opt. Phys.*, vol. 59, no. 4, pp. 2749–2763, 1999.

[55] Y. K. Lee, S. Y. Moon, S. J. Oh, and C. W. Chung, "Determination of metastable level densities in a low-pressure inductively coupled argon plasma by the line-ratio method of optical emission spectroscopy," *J. Phys. D. Appl. Phys.*, vol. 44, no. 28, p. 285203, 2011.

[56] R. Bazinette, J. F. Lelièvre, L. Gaudy, and F. Massines, "Influence of the Discharge Mode on the

Optical and Passivation Properties of SiNx:H Deposited by PECVD at Atmospheric Pressure," *Energy Procedia*, vol. 92, pp. 309–316, 2016.

[57] J. S. Boisvert, J. Margot, and F. Massines, "Transitions of an atmospheric-pressure diffuse dielectric barrier discharge in helium for frequencies increasing from kHz to MHz," *Plasma Sources Sci. Technol.*, vol. 26, no. 3, p. 035004, 2017.

[58] R. Bazinette, J. Paillol, and F. Massines, "Optical emission spectroscopy of glow, Townsend-like and radiofrequency DBDs in an Ar/NH3 mixture," *Plasma Sources Sci. Technol.*, vol. 24, no. 5, p. 55021, 2015.

[59] G. Nayak, M. Simeni Simeni, J. Rosato, N. Sadeghi, and P. J. Bruggeman, "Characterization of an RF-driven argon plasma at atmospheric pressure using broadband absorption and optical emission spectroscopy," *J. Appl. Phys.*, vol. 128, no. 24, p. 243302, 2020.

[60] A. Y. Nikiforov, E. R. Ionita, G. Dinescu, and C. Leys, "Characterization of a planar 8 mm atmospheric pressure wide radiofrequency plasma source by spectroscopy techniques," *Plasma Phys. Control. Fusion*, vol. 58, no. 1, p. 014013, 2015.

[61] J. S. Boisvert, L. Stafford, N. Naudé, J. Margot, and F. Massines, "Electron density and temperature in an atmospheric-pressure helium diffuse dielectric barrier discharge from kHz to MHz," *Plasma Sources Sci. Technol.*, vol. 27, no. 3, p. 035005, 2018.

[62] E. P.J. Linstrom and W.G. Mallard, "NIST Chemistry WebBook, NIST Standard Reference Database Number 69, National Institute of Standards and Technology, Gaithersburg MD, 20899," *NIST Chem. Webb.*

[63] A. V. Pipa, J. Koskulics, R. Brandenburg, and T. Hoder, "The simplest equivalent circuit of a pulsed dielectric barrier discharge and the determination of the gas gap charge transfer," *Rev. Sci. Instrum.*, vol. 83, no. 11, p. 115112, 2012.

[64] F. Massines, N. Gherardi, N. Naudé, and P. Ségur, "Glow and Townsend dielectric barrier

discharge in various atmosphere," *Plasma Phys. Control. Fusion*, vol. 47, no. 12 B, pp. B577–B588, 2005.